Opto-Electronic Advances

ISSN 2096-4579 CN 51-1781/TN

Large-field objective lens for multi-wavelength microscopy at mesoscale and submicron resolution

Xin Xu, Qin Luo, Jixiang Wang, Yahui Song, Hong Ye, Xin Zhang, Yi He, Minxuan Sun, Ruobing Zhang and Guohua Shi

Citation: Xu X, Luo Q, Wang JX, et al. Large-field objective lens for multi-wavelength microscopy at mesoscale and submicron resolution. *Opto-Electron Adv* **7**, 230212(2024).

https://doi.org/10.29026/oea.2024.230212

Received: 20 November 2023; Accepted: 8 April 2024; Published online: 11 June 2024

Opto-Electronic Advances

Article

June 2024, Vol. 7, No. 6

DOI: 10.29026/oea.2024.230212

Large-field objective lens for multi-wavelength microscopy at mesoscale and submicron resolution

Xin Xu[1,2], Qin Luo[1,2], Jixiang Wang[1,2], Yahui Song[1,2], Hong Ye[2], Xin Zhang[2], Yi He[2], Minxuan Sun[1,2], Ruobing Zhang[1,2] and Guohua Shi[1,2]*

Conventional microscopes designed for submicron resolution in biological research are hindered by a limited field of view, typically around 1 mm. This restriction poses a challenge when attempting to simultaneously analyze various parts of a sample, such as different brain areas. In addition, conventional objective lenses struggle to perform consistently across the required range of wavelengths for brain imaging *in vivo*. Here we present a novel mesoscopic objective lens with an impressive field of view of 8 mm, a numerical aperture of 0.5, and a working wavelength range from 400 to 1000 nm. We achieved a resolution of 0.74 μm in fluorescent beads imaging. The versatility of this lens was further demonstrated through high-quality images of mouse brain and kidney sections in a wide-field imaging system, a confocal laser scanning system, and a two-photon imaging system. This mesoscopic objective lens holds immense promise for advancing multi-wavelength imaging of large fields of view at high resolution.

Keywords: mesoscopic objective lens; large field-of-view; high resolution; multi-wavelength; wide-field microscopy; confocal laser scanning microscopy

Xu X, Luo Q, Wang JX et al. Large-field objective lens for multi-wavelength microscopy at mesoscale and submicron resolution. *Opto-Electron Adv* **7**, 230212 (2024).

Introduction

Resolution and field of view (FOV) stand as the two key parameters of a microscope. To improve the imaging resolution, super-resolution microscopy has been proposed, which allows optical imaging at resolutions beyond the diffraction limit[1–5], but as a trade-off, possesses a small FOV, such as several microns in the case of stimulated emission depletion microscopy[2]. Although the resolution has been greatly improved via a series of techniques, the FOV remains constrained due to the inherent design limitations of objective lens. Commercially available objective lenses, capable of submicron resolution imaging, usually exhibit an FOV of approximately 1 mm in diameter. This limited FOV makes it impossible to simultaneously imaging different sections of large samples, which is critical for understanding phenomena such as the early development of mouse embryos[6] or communication between different areas of the mouse brain[7]. Furthermore, the space-bandwidth product (SBP) of these objectives, which refers to the maximum number of pixels that the objective can transfer to the

[1]School of Biomedical Engineering (Suzhou), Division of Life Sciences and Medicine, University of Science and Technology of China, Hefei 230026, China; [2]Jiangsu Key Laboratory of Medical Optics, Suzhou Institute of Biomedical Engineering and Technology, Chinese Academy of Science, Suzhou 215163, China.

*Correspondence: GH Shi, ghshi_lab@sibet.ac.cn

Received: 20 November 2023; Accepted: 8 April 2024; Published online: 11 June 2024

detector[8], is limited to tens of megapixels[9].

To compensate for the limited FOV of commercial microscopy systems, researchers typically capture each FOV sequentially by shifting the sample stage, then stitch the images together to create a comprehensive view of the entire sample[10–12]. However, this approach loses information at the edges of each FOV and is vulnerable to variations across the stitched images due to mechanical displacement of the stage. Most importantly, these sequentially obtained stitched images preclude the possibility to capture simultaneous biological processes in different areas of the sample.

Fourier ptychographic microscopy can offer large-FOV imaging at subcellular resolution[13–15]. In this method, an array of light-emitting diodes (LEDs) is positioned underneath the focal plane of an objective with low numerical aperture (NA) and resolution, yet offers a large FOV. The LEDs successively illuminate the sample from different angles to generate multiple low-resolution images, which are then processed in Fourier space to synthesize a single high-resolution image. However, this method is not suitable for thick samples, fluorescence imaging, or real-time imaging[16].

A light-sheet microscope designed for mesoscopic imaging has been proposed with a maximal FOV of 21 mm[17]. This microscope has shown the ability to image individual axons within a mouse brain. However, it lacks the capability to provide simultaneous high-resolution imaging across its entirety. In contrast, a high-speed microscope with a 12×10 mm^2 FOV has been introduced[18], offering high imaging throughput. But its resolution is insufficient for submicron imaging and the curved imaging plane makes it not easily compatible with other detection systems.

Mesoscopic objective lenses have been described to maintain high NA across the entire FOV, giving submicron resolution over FOV larger than 5 mm, and providing a SBP of 176 megapixels[19–21]. These objectives have a larger volume than conventional objectives. Typically, the aberrations of an objective lens must be controlled within the diffraction limit (Airy Disk). For objective lenses with the same NA, this diffraction limit is a fixed value. However, as FOV expands, aberrations increase exponentially. This implies that optimizing aberrations also becomes much more difficult. Therefore, significantly enlarging the FOV of a conventional objective lens while maintaining the same NA is an extremely challenging task. These mesoscopic lenses offer an SBP that is 10 times greater than conventional objective lenses, demonstrating outstanding aberration optimization. However, these applications cover only the visible (VIS) light band, rendering them unsuitable for two-photon microscopy. This approach, crucial for *in vivo* brain imaging, requires near-infrared (NIR) wavelengths, where these lenses fall short[22–24].

Some mesoscopic objective lenses have been reported for two-photon microscopy, offering FOVs of 3–5 mm and SBPs of 13.7–180 megapixels with working wavelength at NIR[25–29]. However, these objective lenses cannot image with VIS light, making them incompatible with standard one-photon fluorescent imaging. This is crucial as the emission fluorescence is usually in the VIS spectrum and may be affected by aberrations. In addition, although these lens can image across a wavelength range from 900 to 1100 nm, which overlaps with the excitation peaks of enhanced green or yellow fluorescent proteins (900–1000 nm), this range does not encompass the peaks of several other commonly used fluorophores, including cyan fluorescent protein, yellow fluorescent protein, Cy3 or Cy5 (780–900 nm)[30,31].

Here we introduce a groundbreaking mesoscopic objective lens designed to overcome the previously mentioned limitations and challenges. This lens offers an NA of 0.5, an FOV of 8 mm, a working distance of 5 mm, a magnification of 4×, and optimized optical aberration between 400 and 1000 nm. Impressively, it achieves a measured SBP of 367 megapixels and encompasses a wavelength band of 600 nm. This appears to be the greatest throughput and widest wavelength range ever reported for mesoscopic imaging with submicron resolution. Notably, it is the first mesoscopic objective capable of imaging at both VIS and NIR wavelengths. Leveraging this lens, we incorporated it into a wide-field imaging system, a confocal laser scanning imaging system, and a two-photon imaging system. The results from our experiments affirm the lens's exceptional versatility in accommodating different imaging techniques.

Methods and materials

Lens design

The main challenge for achieving a large FOV objective with high-NA lies in optimizing aberration, especially field curvature, distortion, and chromatic aberration. During the lens design process, we used ray-tracing simulation software to select and optimize the primary

location and geometry of the optical components. We computed both on- and off-axis aberrations and optimized the performance by adjusting the element surface radius, materials, space distance, and lens structure. Our mesoscopic objective lens features 10 groups of 19 elements altogether (Fig. 1(a, b),Table 1), with all surfaces spherical for ease of machining. The whole objective system is divided into three lens groups (Fig. 1(a)).

The front group is designed to achieve the demanded NA, meanwhile, minimizing the generation of aberrations. The first cemented doublet (elements 1 and 2) used a quasi-aplanatic design, to limit spherical aberration (SA) and coma to lower values. The material of element 1 (n_d=1.81, ν_d=46.5) and element 2 (n_d=1.7, ν_d=50) has high refractive index and relatively low dispersion. The high refractive index of the front lens can collect large NA with smaller curvature of the surface to reduce the aberrations. Moreover, the low dispersion restricts

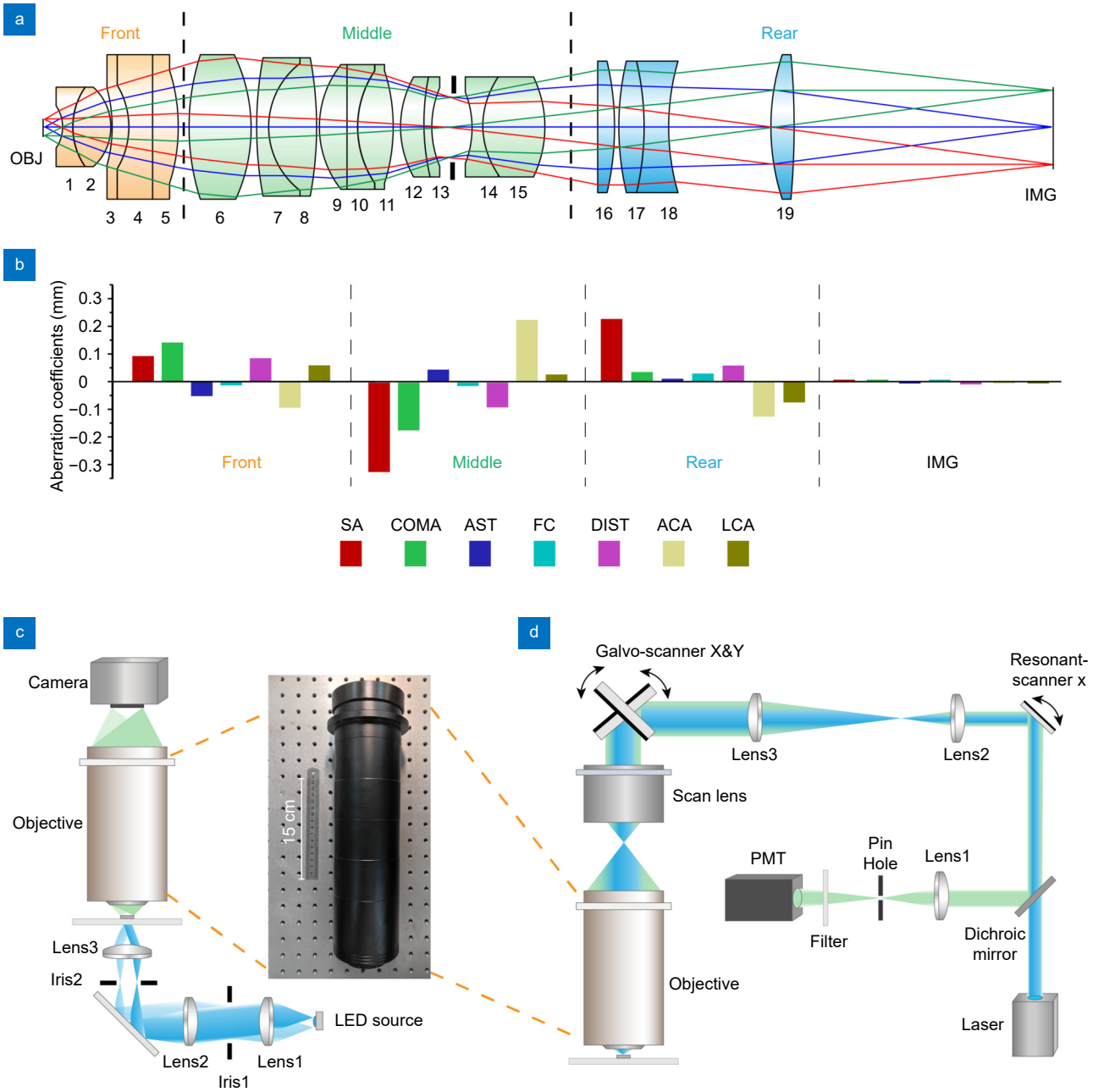

Fig. 1 | (**a**) Structure of the objective lens. (**b**) Aberration coefficients of the three lens groups and the sum of them at the image plane. SA: spherical aberration, AST: astigmatism, FC: field curvature, DIST: distortion, ACA: axial chromatic aberration, LCA: lateral chromatic aberration. (**c**) The wide-field imaging system. (**d**) The confocal laser scanning system.

Table 1 | Design specifications of the objective lens.

Parameters	Value
Field of view (mm)	8
Numerical aperture	0.5
Resolution (μm)*	0.647 (at 530 nm)
Working distance (mm)	5
Wavelength range (nm)	400-1000
Magnification (×)	4
Field curvature (μm)	5
Distortion (%)	0.5
Immersion medium	Water
Telecentricity	Double-sided
Lens surface	All-spherical

* Lateral resolution of the Rayleigh criterion[33], based on an NA of 0.5 over the entire FOV.

the chromatic aberrations. The next cemented triplet is also an aplanatic design to smoothen the ray path. This strategic design of the front lens group significantly alleviates the complexity and design constraints faced by the middle and the rear lens groups.

The middle group is designed to compensate for the aberrations generated by the front group. It consists of one single convex lens, one cemented doublet, one cemented triplet, and two meniscus cemented doublets. The single lens (element 6) characterized by a small curvature, low refractive index, and small dispersion (n_d=1.5, v_d=81.5), inherently produces less aberration on its own. Its main function is to compensate for the machining and assembly error of the whole objective lens by slightly moving this element while assembling the system. The doublet (elements 7 and 8) and triplet (elements 9–11) are primarily designed to address the SA and the axial chromatic aberration (ACA). Particularly, the large curvature of element 8 and element 9 can induce high-order SA to counterbalance the primary SA of the opposite sign. Since the two thick meniscuses (element 12, 13 and element 14, 15) feature a quasi-symmetric structure which can control lateral aberrations such as coma, distortion (DIST), and lateral chromatic aberration (LCA), these two lenses have considerable flexibility to compensate for other aberrations, especially ACA and field curvature (FC) in this design.

The rear group is designed to focus the beam on the image plane and to compensate for all the residual aberrations, especially the LCA which is not fully corrected in the front and middle groups. The cemented doublet (elements 17 and 18) utilized a buried surface design[32], in which the two elements have nearly identical refractive indices but distinctive dispersions. This structure allows for precise control of ACA and LCA by adjusting the curvature of the cemented surface. Additionally, the large air gap between element 18 and element 19 functions as chromatic aberration correction. Because distinct wavelengths have different refractive indices at the same lens element, which have different propagate angles at the same surface, leading to chromatic aberration. After propagating through a large air gap, the margin ray height of beams of different wavelength will be distinctly separated, aiding in the compensation of chromatic aberration.

In our design, SA and coma are controlled by quasi-aplanatic structure in the front group. The middle group mainly compensates for SA, coma, AST, DIST, and ACA. The rear group's focus is on addressing corrections for FC, LCA, and other residual aberrations. In consequence, the aberrations across the entire lens system are fully compensated for through the combination of all three groups (Fig. 1(b)).

Achieving a large FOV with high resolution is not the result of a single structural feature of the objective lens but is an overall outcome. Key aspects to optimize performance of our design include: 1) The structure closest to the object plane must control aberrations as much as possible while achieving the required numerical aperture. To this end, we employed two sets of quasi-aplanatic designs in the front group to significantly reduce spherical and coma aberrations. Additionally, we used cemented lens groups to limit chromatic aberrations. 2) High-order spherical aberrations are generated by employing surfaces with large curvatures to compensate for primary spherical aberrations. As the imaging FOV expands, spherical aberrations sharply increase and become difficult to be compensated for. We applied elements with approximately 40 mm radii of curvature, like element 8 and element 9 in the middle group, to generate high-order spherical aberrations that counteract the primary spherical aberrations. 3) Large air gaps play a critical role in compensating for chromatic aberrations. To achieve imaging across a wide wavelength band from 400 to 1000 nm, adjusting chromatic aberration is critical. In our design, we introduced a large air gap between element 18 and element 19, allowing light of different wavelengths to have distinct ray heights, facilitating the compensation of significant chromatic aberrations.

Most reported mesoscopic objectives are designed for scanning systems, which cannot achieve direct focusing

with a single lens. These approaches require the combination of a tubelens and a scanlens, making the imaging system complex. In contrast, our work can directly focus for imaging with a single objective lens, significantly simplifying the imaging system. Researchers only need to implement sample illumination to easily achieve wide-field imaging, making our system the simplest to image and the most compact in size. Additionally, we have designed a scanning system, as detailed in this manuscript, enabling our objective lens to support both wide-field and scanning imaging.

Addressing the challenge of imaging across visible light and near-infrared wavelengths, conventional objective lens designs have already faced increasing difficulty. Chromatic aberration, especially high-order chromatic aberration, exponentially worsens with the expansion of the FOV. This makes the correction of chromatic aberration extremely challenging for wide-field, wide-band objective lenses. Current related studies only cover one imaging band (see Supplementary information), either VIS or NIR[19,26–29], with some research having an imaging bandwidth of only a few tens of nanometers[26]. In contrast, our objective lens design successfully encompasses the working band from 400 to 1000 nm, including both VIS and NIR. Consequently, our objective lens is the first approach which is compatible with both two-photon imaging operating in the NIR band and one-photon imaging operating in the VIS band. The extensive wavelength range of our objective lens satisfies the needs of most imaging dyes. Therefore, this lens has tremendous potential across diverse biomedical imaging applications.

Wide-field imaging system

We built a wide-field imaging system to verify the imaging performance of our objective lens. As shown in Fig. 1(c), the mesoscopic objective lens was fixed in place using a custom-built brace, and a high-resolution camera (VNP-604MX, Vieworks, Gyeonggi-do, South Korea) was applied as the detector, with the camera sensor positioned in the image plane. The camera sensor measures 14192 × 10640 pixels, with each pixel measuring 3.76 μm, giving a full sensor size of 53.36 × 40.01 mm. This sensor is able to cover the entire image plane, with a diameter of 32 mm. The camera features a “pixel shift mode”, shifting the sensor by one-third of a pixel. The final image is synthesized from nine images, which are shifted relative to one another by one-third of a pixel in the horizontal and vertical directions. In this case, the final image comprises 42576 × 31920 pixels, with each pixel measuring 1.25 μm. Given a 4× magnification from the sample plane to the image plane, the sampling resolution at each pixel in the sample plane is 0.313 μm. Given the theoretical resolution of our objective at 0.647 μm, the Nyquist sampling criterion is satisfied when the camera operates in this pixel shift mode.

For brightfield imaging, the sample slide was mounted on a hollow plate attached to a precision translation stage capable of movements in the *x*, *y*, and *z* directions. The illumination source featured a multi-band LED array equipped with three lenses and an iris to create a Köhler illumination system. Before imaging, a few drops of water were placed on the sample slide, followed by *z*-direction adjustments until the water contacted the objective’s surface. To ensure complete coverage of the entire FOV without air bubbles, additional water was then added between the slide and the objective. Subsequently, the stage was adjusted until the image was focused. This procedure, based on experience, effectively prevent the formation of bubbles in front of the objective while imaging.

During wide-field imaging, the exposure time was set to 20 ms for a single shot, and the maximum frame rate was 6.2 frames per second due to limitations on data readout speed. In the camera's pixel shift mode, the total exposure time extended to 180 ms. However, due to the mechanical movement of the sensor and other influencing factors, the maximum frame rate in this mode decreased to 0.6 frames per second.

During fluorescence imaging, the same multi-band LED array and Köhler system were utilized as in brightfield imaging. The imaging procedure was the same as for brightfield imaging, except that appropriate filters were placed before the LED and camera. The selection of these filters depended on the excitation and emission peaks of the fluorophores to be imaged. Detailed information on this setup is available in the Supplementary information.

To benchmark our objective against commercial ones, we utilized a consistent setup with the same camera and illumination source across all objectives for uniformity. The commercial objectives include a 4× 0.16 NA objective (UPLANSAPO4X, Olympus, Tokyo, Japan) and a 20× 0.5 NA objective (UPLFLN20X, Olympus). The tube lens for these two objectives has a focal length of 200 mm (TTL200-A, Thorlabs, Newton, NJ, United States), giving a 4.4× magnification from the sample plane to the

image plane and a nominal FOV of approximately 6 mm diameter for the 4× 0.16 NA objective, and a 22× magnification from the sample plane to the image plane and a nominal FOV of approximately 1.2 mm diameter for the 20× 0.5 NA objective.

Confocal laser scanning system

To verify the performance of our objective lens in the scanning imaging system, we established a confocal laser scanning system. The schematic diagram of the system is shown in Fig. 1(d). A 488 nm CW fiber laser (W488-25FCD-204, Pavilion Integration Corporation, Suzhou, China) served as the illumination source, with a collimated output beam diameter of 4 mm. This beam was first scanned by a resonant scan mirror resonant-x (CRS12KHz, Novanta, Boston, MA, United States). After a 4-f system consisting of lens2 (SL50-CLS2, Thorlabs) and lens3 (TTL200MP, Thorlabs), the beam diameter was expanded to 16 mm. Next, the beam was scanned by a galvo-scanner pair consists of galvo-X and galvo-Y (S9650, Century Sunny Technology, Beijing, China). Post scanning, the beam was focused by a self-designed scan lens (see Supplementary information) which has a 40 mm diameter scan field, covering the 32 mm image plane of our mesoscopic objective. Afterward, the illumination beam was focused on the sample plane, thus exciting the fluorescence of the sample. The fluorescent signal was reflected by a dichroic mirror (DMSP490R, Thorlabs), and collected by lens1. A pinhole (P100HK, Thorlabs) filtered the non-focal fluorescent signal. Finally, the fluorescent signal was collected by a photomultiplier module (PMT2101, Thorlabs) after passing through a bandpass filter (FBH520-40, Thorlabs).

The resonant and galvo-scanner pairs were all controlled via an analog output device (PCI-6713, National Instruments, Austin, TX, United States). The analog signal of PMT was digitized using a data acquisition card (PCI-5122, National Instruments). For large FOV scanning, the resonant-x scanned 1 mm and the galvo-Y scanned 6 mm at the sample plane, the galvo-X expanded this 6 mm × 1 mm field to 6 mm × 7 mm, yielding a final scanning area of 6 mm × 7 mm at the sample plane with 5400 × 7000 pixels and one pixel size of 1.1 μm × 1 μm. For small FOV scanning, only the resonant-x and the galvo-Y were scanned, with galvo-X fixed at a predetermined position (see Supplementary information). The scan field varied from 100 μm to 1 mm. These scanning parameters including scan field and pixel numbers were particularly selected for the experiments of this paper illustrated in Fig. 6, but are adjustable for different requirements such as a larger scan range or more pixels. The details of the scan strategy are provided in Supplementary information.

Two-photon imaging system

To assess the performance of our objective lens in two-photon imaging, we constructed a two-photon laser scanning microscopy system. A 920 nm femtosecond laser (ALCOR920, Spark lasers, Martillac, France) served as the illumination source. The resonant scanner and galvo scanner are identical to those used in the previously described confocal laser scanning system. It is notable that our two-photon imaging system constitutes part of a multi-channel synchronous imaging system currently in development. We employed diffractive elements to divide the illumination light and executing synchronous scanning, enabling multi-channel synchronous detection. This method significantly increases imaging speed, addressing the prevalent challenge of slow speed (typically only a few FPS) in mesoscopic two-photon imaging. As this study is in its preliminary research phase, a detailed system diagram is not provided. The spatial dispersion caused by diffraction between channels has yet to be effectively resolved. Imaging outcomes from the central channel, which corresponds to zero-order light, are superior. However, results from peripheral channels, associated with higher-order diffracted light, are adversely affected by dispersion-related spot blurring and pulse broadening. These challenges will be solved in our future work. For the present, we only present the two-photon imaging results of the central channel. The achieved imaging FOV is 1 mm × 6 mm with a resolution of 1000 × 5400 pixels.

Sample preparation

All experiments were performed according to the Guidelines for Animal Experimentation of the Animal Experimentation Ethics Committee of the Suzhou Institute of Biomedical Engineering and Technology, Chinese Academy of Science. Brains were removed from 2-month-old C57BL/6J mice (Vital River Laboratories, Beijing, China) and sectioned to a thickness of 6 μm. The sections were fixed in ice-cold 4% paraformaldehyde (catalog no. J61899-AK, Thermo Fisher Scientific, Waltham, MA, USA), stained using hematoxylin-eosin (catalog no. C0105S, Beyotime, Shanghai, China), then

mounted onto a glass microscope slide (catalog no. 188105, Citotest, Nantong, China) using Vectashield mounting medium (catalog no. H-1200, Vector Laboratories, Newark, CA, USA). The slice of kidney tissue was commercially prepared (FluoCells™ Prepared Slide #3, catalog no. F24630, Thermo Fisher Scientific). The slice of bovine pulmonary artery endothelial (BPAE) cells was commercially prepared (FluoCells™ Prepared Slide #1, catalog no. F36924, Thermo Fisher Scientific). All the slides were imaged with water immersion.

Results and discussion

To achieve a large FOV, the lenses within our objective are several times larger than those in conventional objective lenses, featuring a maximum diameter of 70 mm and a length of 347 mm. The maximum diameter of the lens elements is determined by the ray height, such as element 6 (68 mm diameter) and element 19 (70 mm diameter). This factor makes it difficult to reduce the diameter of the objective lens. Additionally, for aberration optimization, it's challenging to reduce the number of lens elements in between. The current structure, a result of multiple iterations, is already difficult to simplify further, making it challenging to reduce the length of the objective lens.

A significant application of mesoscopic imaging lies in neuroscience imaging, enabling high-resolution imaging of various brain regions in mice. No matter the imaging is *in vivo* or *in vitro* (such as the recent research focus on whole mouse brain imaging with tissue clearing), the refractive index of water is closer to that of biological samples. Opting for an air objective lens, where a significant refractive index difference exists between the medium and the sample, would introduce spherical aberrations. These aberrations are difficult to avoid and would worsen with changes in the imaging depth of the sample. Given the potential emphasis on neuroscience imaging for our objective, we intentionally chose to design a water-immersion lens to address these concerns.

In the lens design, we optimized the field curvature to below 5 μm and kept distortion under 0.5% across the entire FOV. The chromatic focal shift was maintained below 6 μm across the entire working range of wavelengths from 400 to 1000 nm. The objective provides a 4× magnification from the sample plane to the image plane, ensuring the 32 mm diameter image plane to be detected by commercially available camera sensors. The high Strehl ratios of the system (Fig. 2(a)) indicate good correction. Notably the on-axis Strehl ratio exceeds 0.9 over the entire working wavelength range (Table 2), which surpasses the diffraction limit ratio of 0.8.

Simulated field curvature remains below 5 μm across the entire working wavelength range. Particularly, it stays within 4 μm for wavelength ranging from 500 to 1000 nm (Fig. 2(b)). Distortion increases with the height of the image field, yet the maximum distortion is confined to 0.5% at the edge of the field (Fig. 2(c)).

When the primary wavelength is set at 530 nm, the focal shift between 500 and 1000 nm is limited to ± 2 μm, while the shift between 400 and 500 nm is confined to ± 6 μm (Fig. 2(d)). This indicates good control of chromatic aberration, suitable for simultaneous imaging of multiple colors.

The objective lens is designed to be a double-sided telecentric lens. Telecentricity is important for ensuring constant image size with sample depth in a laser scanning imaging system[34,35]. Image size should remain constant for the different layers of the sample, despite the presence of focus-adjusting elements in the laser scanning microscope system, such as electronically tunable lenses[36] or a remote focus system[37]. Telecentricity is also vital for two-photon imaging, in which the excitation beam is scanned across the entire FOV to guarantee high peak power at the focus. In this situation, the scan lens, which is positioned after the scan device, needs to be telecentric in order to align with the image plane. Without telecentricity, significant aberration would occur where the scan lens and the objective lens overlap. The simulated telecentricity of our objective is below 0.13° at the image space and less than 0.3° at the objective space (Table 3). These parameters indicate that the objective can image different sample layers at a constant magnification, enhancing its suitability for scanning.

After optimizing the design and construction of our mesoscopic objective, we conducted tests using a USAF 1951 high-resolution positive test target under wide-field illumination (Fig. 2(e)). Even the thinnest bar was recognizable (Fig. 2(f)) in a region of 645 line pairs per mm (lp/mm), where each bar was 0.775 μm in width. Furthermore, with a custom-designed negative resolution test target, the objective lens was able to resolve bars of 0.7 μm (Fig. 2(f)). This indicates a wide-field resolution better than 714 lp/mm. Figure 2(g) shows the intensity distribution along the red line in Fig. 2(f). The normalized intensity of the bright stripe was I_{max}=1, and the dark stripe was I_{min}=0.471, resulting in a contrast of

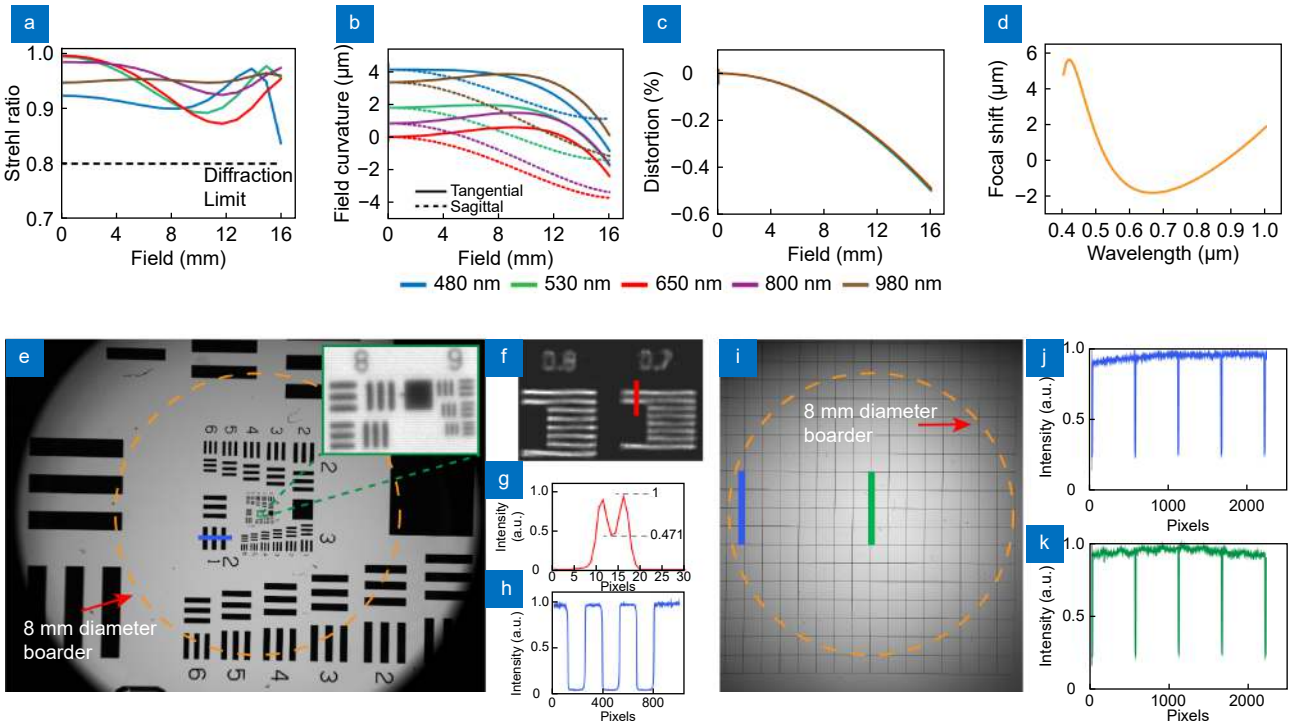

Fig. 2 | (**a**) Strehl ratio of the lens. The center of the image plane lies at 0 mm, while the edge of the image plane in one direction lies at 16 mm. (**b**) Field curvature in the tangential plane (solid lines) and sagittal plane (dashed lines) over the entire image field at different wavelengths. (**c**) Distortion across the image field. (**d**) Focal shifts at different wavelengths. Data at (a)-(d) are obtained from the ray-tracing software (Opticstudio, Zemax). (**e**) Wide-field transmission imaging of a USAF 1951 target. (**f**) Zoomed-in of a custom-built negative resolution target. (**g**) Intensity spreading of red lines in panel (f). (**h**) Intensity spreading of blue lines in group 2 / element 1 in panel (e). (**i**) Imaging of a grid test target. (**j**) Intensity spreading of blue lines at the margin of the nominal FOV. (**k**) Intensity spreading of green lines in the center of the nominal FOV.

Table 2 | Strehl ratio of the objective lens at different wavelengths.

Wavelength (nm)	Strehl ratio	
	On-axis	Full field
480	0.92	0.83
530	0.99	0.89
650	0.99	0.87
800	0.98	0.92
980	0.94	0.94

Table 3 | Telecentricity based on the chief ray angle at different fields.

Normalized field*	Chief ray angle (°)	
	at image plane	at sample plane
0	0	0
0.3	0.082	0.061
0.5	0.12	0.110
0.7	0.129	0.170
1	0.057	0.297

* Fields are designated based on their distance from the center of the field of view: 0 refers to the center, 1 to the edge.

$(I_{max}-I_{min})/(I_{max}+I_{min})=0.35$. In the simulated modulation transfer function (MTF) of our objective (see Supplementary information), when the MTF curve reaches a contrast of 0.35, the theoretically distinguishable stripe period is 771 lp/mm, which roughly aligns with our test result of 714 lp/mm.

We determined an FOV of 8 mm given the objective's ability to image the bar of group 2 / element 1 of the positive test target, which consists of 4 line pairs per mm. And the full width at half maximum (FWHM) was 670

pixels (Fig. 2(h)). Consequently, one pixel in the image covered 0.932 μm of the sample plane, meaning the entire image size of 14196 × 10640 pixels corresponded to an area of 13.2 × 9.9 mm.

We measured distortion by imaging a grid test target (Fig. 2(i)) with the wide-field imaging system. Given an image of 14192 × 10640 pixels, where one pixel covers 0.94 μm at the sample plane, the circle diameter of 8510 pixels corresponds to an FOV diameter of 8 mm. Plotting the intensity spreading lines at the center and the edge of the FOV revealed that the four-grid pattern covered 2181 pixels at the center of the FOV (Fig. 2(k)) and 2191 pixels at the edge (Fig. 2(j)), indicating a distortion of 10 pixels (0.46%). We measured the distortion slightly away from the margin of the FOV, given that the most marginal distortion of a circular FOV cannot be determined due to difficulties in precise pixel count measurement along a line.

Next, we imaged a slide covered with the same fluorescent beads in order to assess field curvature. The slide was placed on the precision translation stage, which we adjusted until the center of the FOV was in focus, giving a clear image of the beads. Then the stage was adjusted to bring the upper edge of the FOV into focus, giving a clear image. The difference in stage position between the center and edge of the FOV indicated a field curvature of

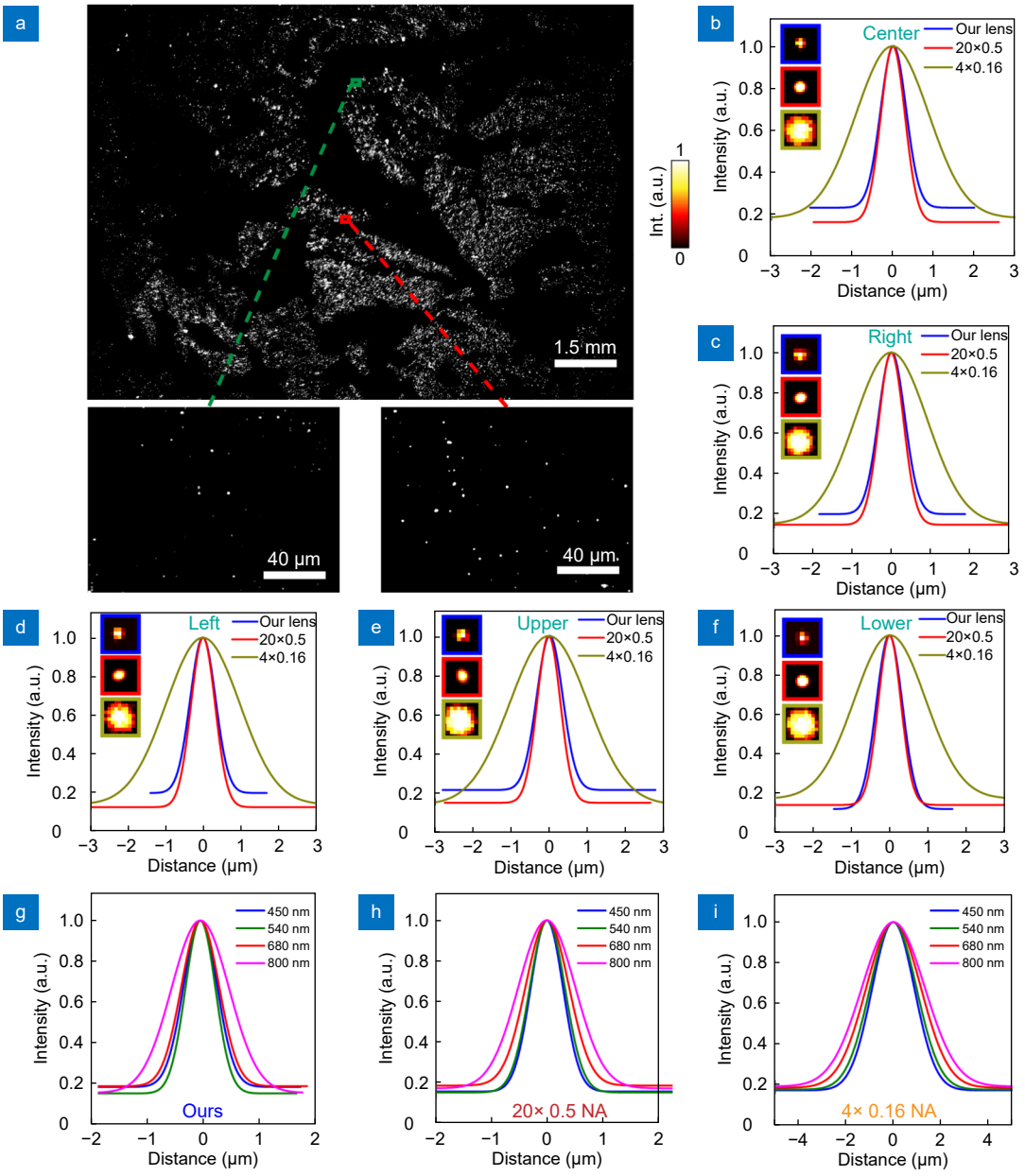

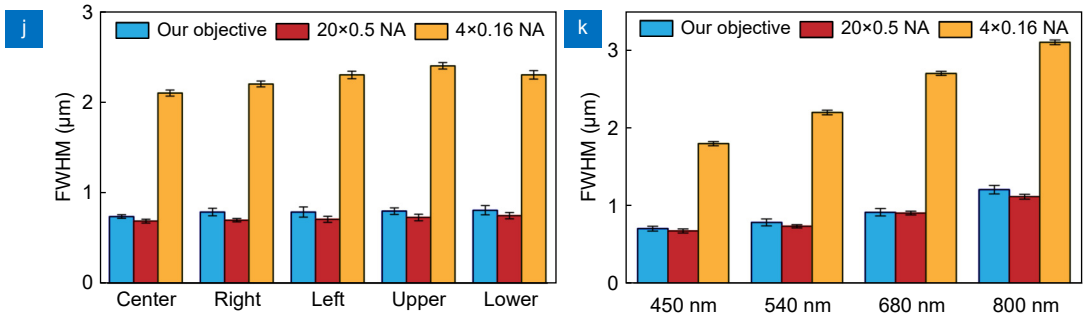

Fig. 3 | (**a**) Imaging of beads with a diameter of 500 nm across the entire FOV. (**b**) The FWHM results of microspheres in the central imaging field for the three objectives. (**c**) The FWHM results of microspheres in the right field area for each objective. (**d**) The FWHM results of microspheres in the left field area for each objective. (**e**) The FWHM results of microspheres in the upper field area for each objective. (**f**) The imaging results of microspheres in the lower field area for each objective. (**g**) The FWHM results for microspheres fluorescing at different wavelengths using our objective lens. (**h**) The FWHM results for microspheres fluorescing at different wavelengths using the 20× 0.5 NA objective. (**i**) The FWHM results for microspheres fluorescing at different wavelengths using the 4× 0.16 NA objectives. (**j**) The FWHM of microspheres in different field areas for the three objectives (mean ± SEM, n = 7 beads), with our lens achieving 0.74 ± 0.02 μm, 0.79 ± 0.042 μm, 0.79 ± 0.055 μm, 0.8 ± 0.036 μm, 0.81 ± 0.051 μm. The 20× 0.5 NA objective results were 0.69 ± 0.021 μm, 0.7 ± 0.018 μm, 0.71 ± 0.033 μm, 0.73 ± 0.036 μm, 0.75 ± 0.034 μm. The 4× 0.16 NA objective results were 2.1 ± 0.033 μm, 2.2 ± 0.032 μm, 2.3 ± 0.041 μm, 2.4 ± 0.037 μm, 2.3 ± 0.047 μm. (**k**) The FWHM results of microspheres at different wavelengths (mean ± SEM, n = 7 beads) for each objective. At 450 nm, 540 nm, 680 nm, and 800 nm imaging, our lens achieved 0.71 ± 0.032 μm, 0.79 ± 0.045 μm, 0.92 ± 0.048 μm, 1.21 ± 0.054 μm. The 20× 0.5 NA objective results were 0.68 ± 0.027 μm, 0.74 ± 0.032 μm, 0.91 ± 0.034 μm, 1.12 ± 0.051 μm. The 4× 0.16 NA objective results were 1.8 ± 0.038 μm, 2.2 ± 0.059 μm, 2.7 ± 0.036 μm, 3.1 ± 0.061 μm.

7 μm.

We benchmarked our objective against two commercial objectives using identical samples, camera, and illumination setups. The first was a 4× 0.16 NA objective (UPLANSAPO4X, Olympus), with the same magnification and a smaller FOV (6 mm) compared to our objective. The second was a 20× 0.5 NA objective (UPLFLN20X, Olympus), matching our objective's NA but offering a much smaller FOV (1.2 mm) though at roughly similar resolution as our objective. Figure 3(b–f) compare the imaging results of 500 nm microspheres at different FOVs for the three objectives. Our objective, with an 8 mm FOV, is represented by "center" for the imaging situation in the central FOV, "Right" for imaging results about 4 mm to the right of the center, "Left" for results about 4 mm to the left of the center, "Upper" for results about 4 mm above the center, and "Lower" for results about 4 mm below the center. The 20× 0.5 NA commercial objective, with a 1.2 mm FOV, is represented by “center” for the central FOV, "Right," "Left," "Upper," and "Lower" for imaging results approximately 0.6 mm from the center in the respective directions. The 4× 0.16 NA commercial objective, with a 6 mm FOV, is represented by “center” for the central FOV, and "Right," "Left," "Upper," and "Lower" for imaging results approximately 3 mm from the center in the respective directions.

Figure 3(g–i) present the imaging results of the three objectives when microsphere fluorescence is excited at different wavelengths. Figure 3(j) shows the FWHM (mean ± SEM, n = 7 beads) of microspheres in five different FOVs for the three objectives. Specifically, our objective achieved results of 0.74 ± 0.02 μm, 0.79 ± 0.042 μm, 0.79 ± 0.055 μm, 0.8 ± 0.036 μm, and 0.81 ± 0.051 μm. The 20× 0.5 NA objective yielded results of 0.69 ± 0.021 μm, 0.7 ± 0.018 μm, 0.71 ± 0.033 μm, 0.73 ± 0.036 μm, and 0.75 ± 0.034 μm. The 4× 0.16 NA objective exhibited results of 2.1 ± 0.033 μm, 2.2 ± 0.032 μm, 2.3 ± 0.041 μm, 2.4 ± 0.037 μm, and 2.3 ± 0.047 μm. Figure 3(k) shows the FWHM (mean ± SEM, n = 7 beads) of microspheres at different wavelengths for the three objectives, with our objective results at 450 nm, 540 nm, 680 nm, 800 nm imaging being 0.71 ± 0.032 μm, 0.79 ± 0.045 μm, 0.92 ± 0.048 μm, and 1.21 ± 0.054 μm respectively. The 20× 0.5 NA objective showed results of 0.68 ± 0.027 μm, 0.74 ± 0.032 μm, 0.91 ± 0.034 μm, and 1.12 ± 0.051 μm. The 4× 0.16 NA objective displayed results of 1.8 ± 0.038 μm, 2.2 ± 0.059 μm, 2.7 ± 0.036 μm, and 3.1 ± 0.061 μm. The tested efficiency of our lens is about 60% at VIS wavelengths and about 75% at NIR wavelengths.

Finally, we employed the objective lens to image slices of biological samples in both the wide-field imaging system (Figs. 4, 5) and the laser scanning imaging system (Figs. 6, 7). In wide-field imaging, we imaged the mouse brain and kidney slices. The imaging of the brain slice revealed clear, distinct cells across the entire FOV (Fig. 4(a)). The kidney section was stained simultaneously

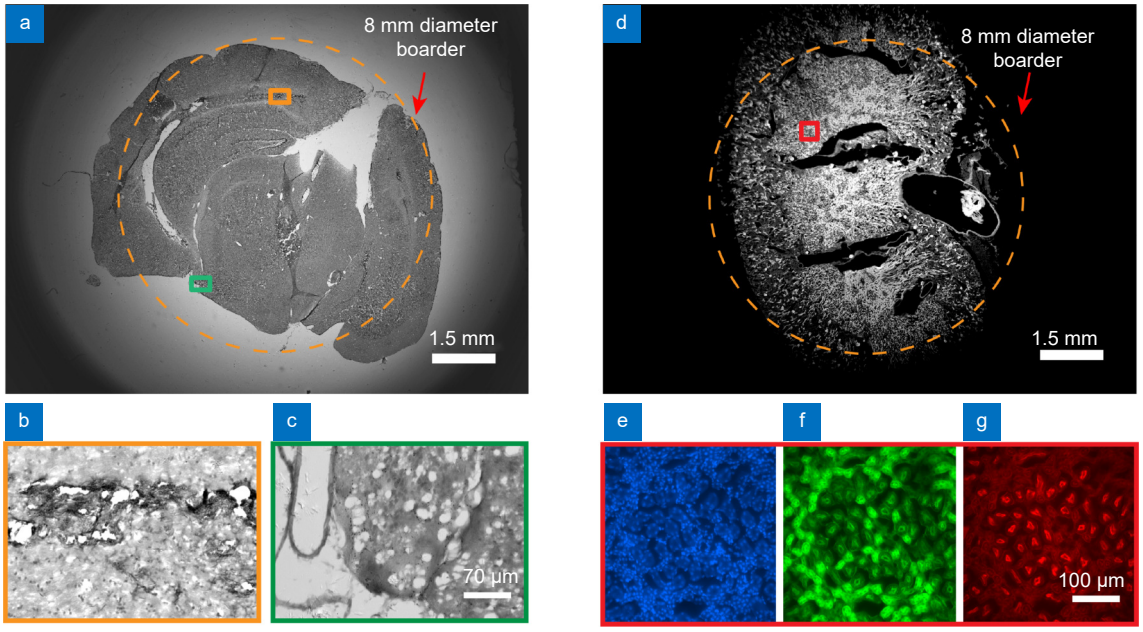

Fig. 4 | Wide-field imaging of mouse brain and kidney. (**a**) Brightfield imaging of mouse brain slice with our objective lens. Scale bar, 1.5 mm. Though the effective FOV with aberration optimization is 8 mm, FOVs slightly larger than 8 mm can also be imaged. Thus, the entire FOV is slightly larger than the nominal diameter of 8 mm. (**b**) Zoomed-in view of the yellow rectangle part of the panel (a). (**c**) Zoomed-in view of the green rectangle part of the panel (a). (**d**) Fluorescence imaging of a mouse kidney slice after simultaneous labeling with Alexa Fluor 488, Alexa Fluor 568, and DAPI, showing Alexa Fluor 488 labeling (excitation wavelength, 490 nm; emission wavelength, 515 nm). (**e**) Zoomed-in view of the red rectangle part of the panel (d), showing DAPI labeling (excitation, 380 nm; emission, 455 nm). (**f**) The same image zone as in panel (e), showing Alexa Fluor 488 labeling. (**g**) The same image zone as in panel (e), showing Alexa Fluor 568 labeling (excitation, 540 nm; emission, 600 nm).

with three fluorescent dyes: Alexa Fluor 488-conjugated wheat germ agglutinin to label glomeruli and convoluted tubules, Alexa Fluor 568-conjugated phalloidin to label filamentous actin in glomeruli and the brush border, and DAPI to label nuclei. The entire tissue slice was captured in a single frame (Fig. 4(d)), indicating the potential of our objective for high-resolution, multi-labeling of large samples, such as multi-color neuronal activity recording[38]. We benchmarked our objective against two commercial objectives (Fig. 5) using the same biological samples and camera and illumination setup. The 4× 0.16 NA objective (UPLANSAPO4X, Olympus), with the same magnification and a smaller FOV (6 mm) than our objective, displayed substantially inferior resolution. The FOV of this 4× 0.16 NA objective is outlined with a red dashed line in Fig. 5(a, c, g, i). The 20× 0.5 NA objective (UMPLFLN20X, Olympus), matching our objective's NA but offering a much smaller FOV (1.2 mm) though at roughly similar resolution as our objective. The FOV of this 20× 0.5 NA objective is marked with a cyan dashed line in Fig. 5(a, b, g, h). To quantitatively compare the imaging performance of our objective lens with commercial ones, we analyzed the same imaging areas across different lenses in Fig. 5(d–f) and 5(j–l). We employed three image clarity evaluation functions as assessment metrics: the Brenner function, the Energy of Gradient (EOG) function, and the Tenengrad function[39,40]. The normalized results for the clarity of structural imaging of mouse brain slices and fluorescence imaging of kidney slices are shown in Fig. 5(m) and 5(n). The commercial 20× 0.5 NA objective lens displayed the best imaging performance. While our objective lens slightly underperformed compared to this lens, it significantly surpassed the imaging quality of the 4× 0.16 NA commercial objective lens with a similar field of view (FOV = 6 mm). It is important to note that the 20× 0.5 NA lens has a magnification of 20 times, resulting in a sampling rate five times higher than that of our lens for the imaging results shown in Fig. 5(e) and 5(k). This difference in sampling rate might contribute to the slightly lower imaging clarity of our lens. Nevertheless, this comparison suggests that our objective shows excellent potential for imaging large FOVs at high resolution.

While the FOV available for high-resolution imaging with our objective lens is 8 mm, it has the capability to capture a wider area up to 12 mm. This extended coverage is based on a camera sensor of 53 mm × 40 mm, and a 4 × magnification from the objective plane to the

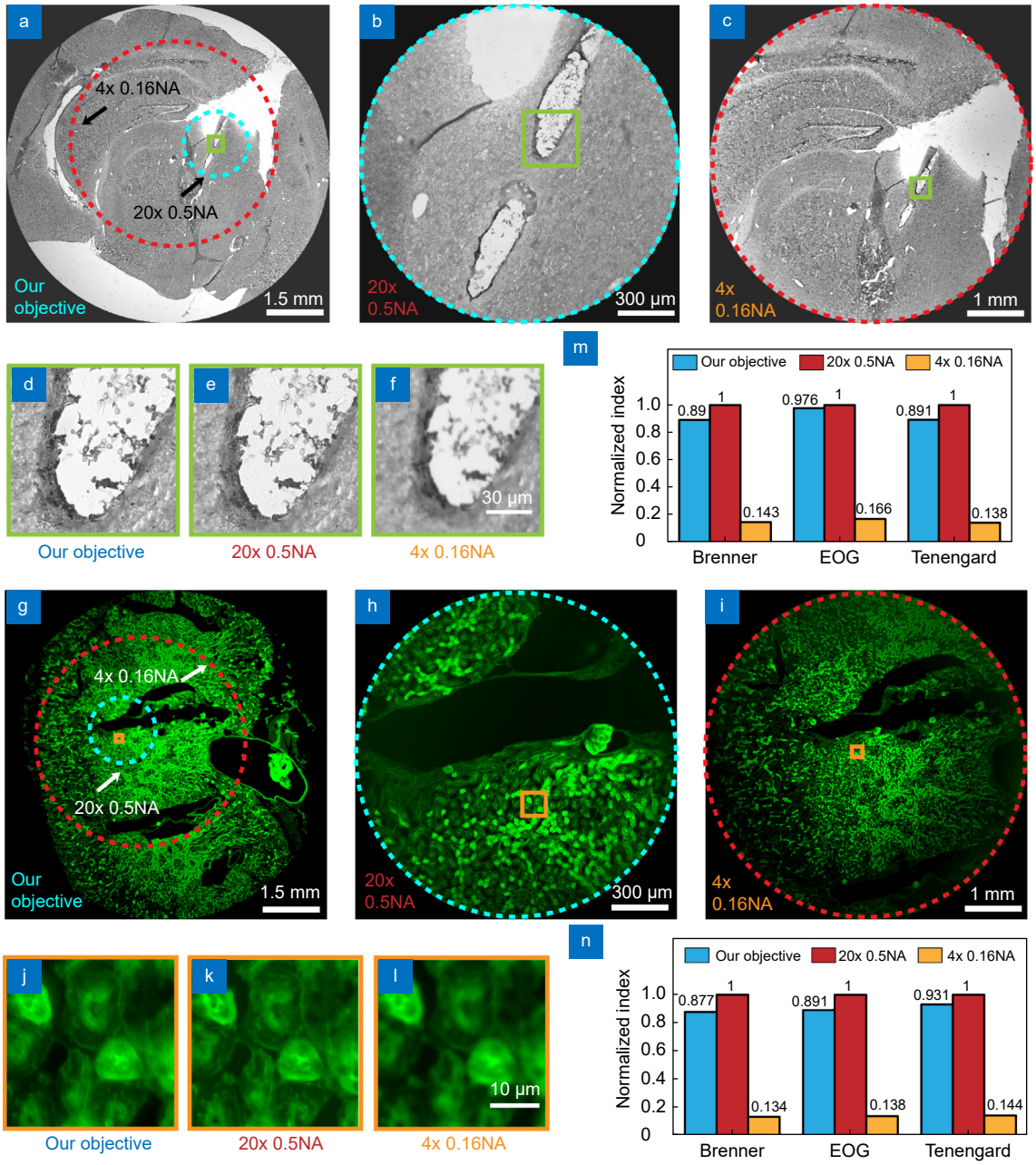

Fig. 5 | Wide-field imaging comparison between our objective and commercial objectives. (**a**) Brightfield imaging of a mouse brain slice with our objective lens at a nominal FOV. (**b**) Brightfield imaging of a mouse brain slice with a commercial 20× 0.5 NA objective lens (UPLFLN20X, Olympus) at nominal FOV of about 1.2 mm diameter. (**c**) Brightfield imaging of a mouse brain slice with a commercial 4× 0.16 NA objective lens (UPLANSAPO4X, Olympus) at a nominal FOV of about 6 mm diameter. (**d**) Zoomed-in view of part of the panel (a). (**e**) Zoomed-in view of part of the panel (b). (**f**) Zoomed-in view of part of the panel (c). Scale bar: 30 μm in panels (d–f). (**g**) Fluorescence imaging of a mouse kidney slice with our lens at nominal FOV, showing Alexa Fluor 488 labeling. (**h**) Fluorescence imaging of mouse kidney slice with a commercial 20× 0.5 NA objective at nominal FOV. (**i**) Fluorescence imaging of a mouse kidney slice with a commercial 4× 0.16 NA objective at nominal FOV. (**j**) Zoomed-in view of part of the panel (g). (**k**) Zoomed-in view of part of the panel (h). (**l**) Zoomed-in view of part of the panel (i). Scale bar: 10 μm in panels (j–l). (**m**) The results of image clarity analysis for (d–f). (**n**) The results of image clarity analysis for (j–l).

image plane, resulting in a full detection field of about 13.3 mm × 10 mm (Fig. 4). However, the aberrations between 8 and 12 mm have not yet been optimized, which will be a focus of our future work. Even though this region may not provide high-resolution imaging, it can still be useful for sample positioning.

Compared with the 20× 0.5 NA commercial objective, our objective lens offers a substantially larger FOV with similar resolution. However, a few details are lost especially in the low-contrast area of the sample. This is

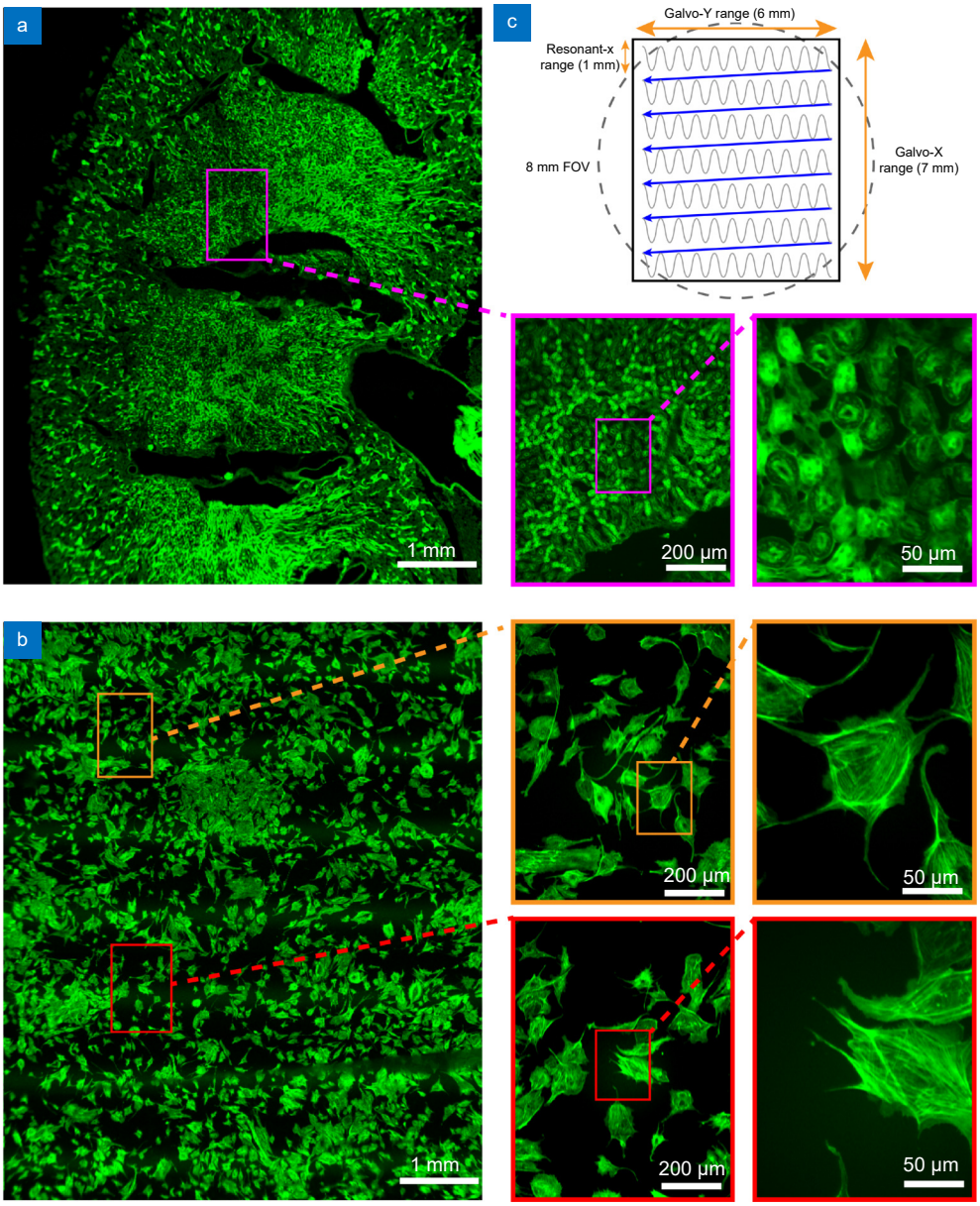

Fig. 6 | Confocal laser scanning imaging results. (**a**) Imaging of mouse kidney slice. (**b**) Imaging of BPAE cells slice. The whole field images in (a) and (b) were scanned by all 3 scanners, these images are 5400 × 7000 pixels, and the pixel sizes are 1.1 μm × 1 μm. The zoomed-in images were scanned by resonant-x and galvo-Y scanners, they are 800 × 1000 pixels. The pixel size of the first zoomed-in image is 0.9 μm × 0.9 μm, and the further zoomed-in ones are 0.23 μm × 0.23 μm. (**c**) Scanning pattern of whole field imaging in (a) and (b). Resonant-x scans at 12 kHz. Galvo-Y scans at 2 Hz, and one cycle contains 6000 resonant-x cycles, and 10% of these cycles are at the scan-back duration of galvo-Y. Therefore, only 5400 resonant-x cycles are effective for imaging. One galvo-X scan cycle has only 7 positions and contains 7 galvo-Y cycles.

primarily because our objective (4×) has a 5 times lower magnification than the commercial one (20×), leading to a much lower sampling rate with the same detection camera. Although our imaging meets the Nyquist sampling criterion, its performance is not as high as that with a 5-times higher sampling rate. The working distance of our objective lens is 5 mm, in contrast to the approximately 2–3 mm of commercial 0.5 NA objective lenses. This extended working distance allows enough space for deep imaging of thicker samples. This may be particularly beneficial for studies involving optical tissue clearing, reducing the need for sample slicing[42,43].

In confocal laser scanning imaging. We scanned a 6 mm × 7 mm FOV as Fig. 6(c) shows. The resonant-x scanner covered a 1 mm distance on the sample plane at 12 kHz, the galvo-Y scanner covered a 6 mm distance on the sample plane at 2 Hz, the galvo-X scanner scanned 1 mm with each end cycle of galvo-Y, totaling a 7 mm scan

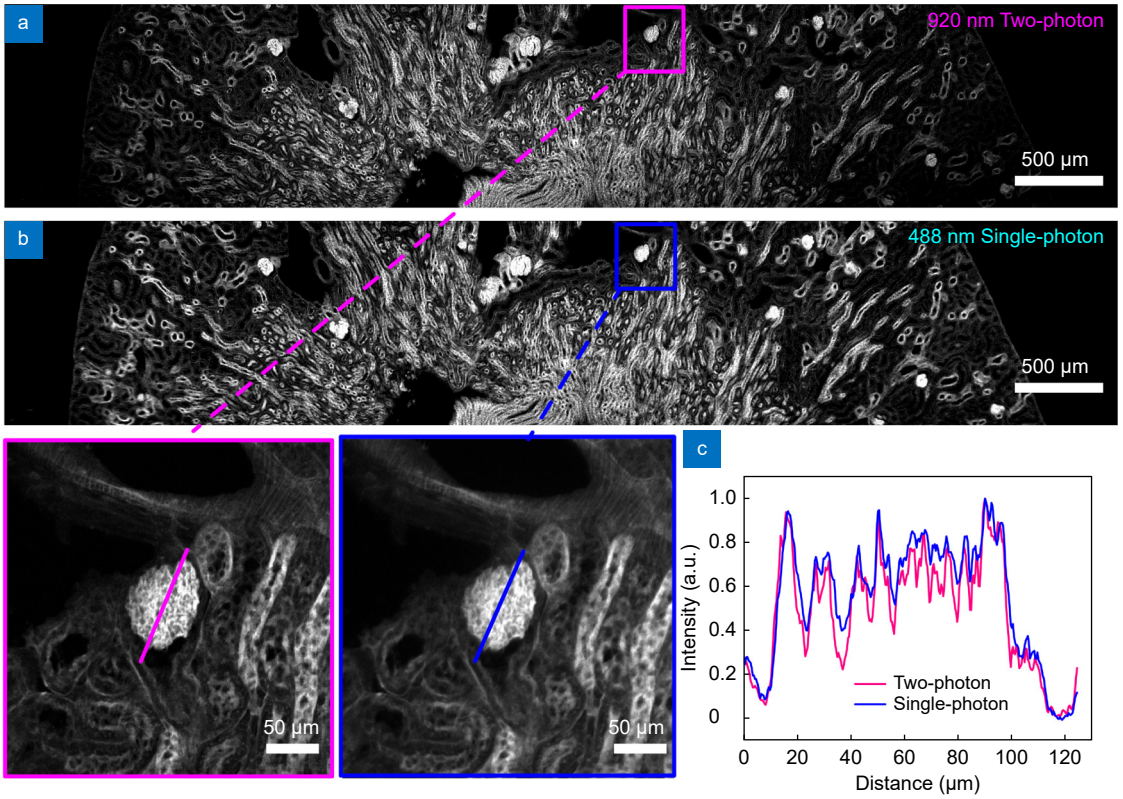

Fig. 7 | (**a**) The two-photon imaging results of a mouse kidney slice when excited with a 920 nm femtosecond laser using our objective lens. (**b**) The single-photon imaging results of a mouse kidney slice under the same system, except using a 488 mm continuous-wave laser for excitation. The whole field images in (a) and (b) are 5400 × 1000 pixels, with pixel sizes of 1.1 μm × 1 μm. The zoomed-in images are 900 × 1000 pixels, with pixel sizes of 0.36 μm × 0.36 μm. (**c**) The intensity distribution curves of the same glomerular region in both imaging results.

range for galvo-X. The sample of a mouse kidney is imaged the same as wide-field imaging. The BPAE cells in which F-actin was stained with Alexa Fluor™ 488 phalloidin were imaged in Fig. 6(b). The zoomed-in images in Fig. 6(a) and 6(b) were captured with the galvo-X fixed, while the galvo-Y and the resonant-x scanned the specific rectangular range.

In two-photon laser scanning imaging, we scanned a 6 mm × 1 mm FOV as Fig. 7(a) shows. The resonant-x scanner covered a 1 mm distance on the sample plane at 12 kHz, while the galvo-Y scanner covered a 6 mm distance on the sample plane at 2 Hz. The imaging sample was another mouse kidney section labeled with Alexa Fluor 488. We conducted single-photon imaging using the same system, by replacing the 920 nm femtosecond laser with a 488 nm continuous-wave laser as the excitation light, as shown in Fig. 7(b). The zoomed-in images in Fig. 7(a) and 7(b) were captured with the galvo-Y and the resonant-x scanning the specific rectangular range. The zoomed-in results in Fig. 7(c) presents the grayscale distribution curve of a glomerulus. The comparison with single-photon imaging reveals that two-photon imaging offers higher contrast, attributed to the nonlinear excitation effect of two-photon imaging, which results in a more concentrated excitation focus. This effectively demonstrates the two-photon imaging capabilities of our objective lens.

Conclusions

We have developed a mesoscopic objective lens with an FOV of 8 mm, a NA of 0.5, a working distance of 5 mm in water, and a measured SBP of 367 megapixels. Optical aberration is optimized in the VIS-NIR range from 400 to 1000 nm. These characteristics make our objective lens promising for diverse multi-label, real-time studies of biological processes that occur over longer distances in tissue, such as examining communication between different parts of the brain or tracking morphological and biochemical changes during embryonic development. The objective lens is also compatible with two-photon microscopy, which is currently the most powerful tool for *in vivo* brain imaging[41]. To our knowledge, our objective lens has the largest FOV in submicron resolution imaging and is the first mesoscopic objective lens to

image across the VIS to NIR spectrum .

Our mesoscopic objective lens demonstrates excellent potential for simultaneous multi-channel monitoring of short-, mid-, and long-range biological processes in samples. The objective is compatible with both one- and two-photon imaging setups, which together support most biological imaging studies. Future work will focus on functional imaging of multiple brain regions in mice *in vivo* with this objective lens. Another goal is to develop a wider wavelength lens that covers the NIR-II spectrum, which is an important wavelength band for *in vivo* in-depth imaging[44]. Finally, the ultimate goal is to realize ultra-wide wavelength coverage, large FOV, significant depth, and high-resolution imaging. Another potential development direction is to combine our objective lens with Fourier Ptychographic Microscopy (FPM). FPM is typically employed with low NA lenses (usually 0.1 NA) and synthesizes hundreds or even thousands of images into a single high-resolution image, equivalent to one obtained with a high NA lens (typically around 1 NA). Our objective lens, featuring a relatively large imaging FOV and a higher NA of 0.5, indicates that fewer imaging iterations are required to achieve a resolution comparable to a 1 NA lens. Consequently, integrating our lens with FPM could significantly improve imaging speed. This method is particularly promising for applications that demand a large FOV, extremely high resolution, and fast imaging speeds.

References

1. Sigal YM, Zhou RB, Zhuang XW. Visualizing and discovering cellular structures with super-resolution microscopy. *Science* **361**, 880–887 (2018).
2. Westphal V, Rizzoli SO, Lauterbach MA et al. Video-rate far-field optical nanoscopy dissects synaptic vesicle movement. *Science* **320**, 246–249 (2008).
3. Rust MJ, Bates M, Zhuang XW. Sub-diffraction-limit imaging by stochastic optical reconstruction microscopy (STORM). *Nat Methods* **3**, 793–796 (2006).
4. Abraham E, Zhou JX, Liu ZW. Speckle structured illumination endoscopy with enhanced resolution at wide field of view and depth of field. *Opto-Electron Adv* **6**, 220163 (2023).
5. Xiao YT, Chen LW, Pu MB et al. Improved spatiotemporal resolution of anti-scattering super-resolution label-free microscopy via synthetic wave 3D metalens imaging. *Opto-Electron Sci* **2**, 230037 (2023).
6. Huang Q, Cohen MA, Alsina FC et al. Intravital imaging of mouse embryos. *Science* **368**, 181–186 (2020).
7. Yang MK, Zhou ZQ, Zhang JX et al. MATRIEX imaging: multi-area two-photon real-time in vivo explorer. *Light Sci Appl* **8**, 109 (2019).
8. Lohmann AW, Dorsch RG, Mendlovic D et al. Space–bandwidth product of optical signals and systems. *J Opt Soc Am A* **13**, 470–473 (1996).
9. Pan A, Zuo C, Yao BL. High-resolution and large field-of-view Fourier ptychographic microscopy and its applications in biomedicine. *Rep Prog Phys* **83**, 096101 (2020).
10. Economo MN, Clack NG, Lavis LD et al. A platform for brain-wide imaging and reconstruction of individual neurons. *eLife* **5**, e10566 (2016).
11. Hörl D, Rojas Rusak F, Preusser F et al. BigStitcher: reconstructing high-resolution image datasets of cleared and expanded samples. *Nat Methods* **16**, 870–874 (2019).
12. Voleti V, Patel KB, Li WZ et al. Real-time volumetric microscopy of in vivo dynamics and large-scale samples with SCAPE 2.0. *Nat Methods* **16**, 1054–1062 (2019).
13. Tian L, Liu ZJ, Yeh LH et al. Computational illumination for high-speed *in vitro* Fourier ptychographic microscopy. *Optica* **2**, 904–911 (2015).
14. Lee H, Chon BH, Ahn HK. Reflective Fourier ptychographic microscopy using a parabolic mirror. *Opt Express* **27**, 34382–34391 (2019).
15. Song S, Kim J, Hur S et al. Large-area, high-resolution birefringence imaging with polarization-sensitive Fourier ptychographic microscopy. *ACS Photonics* **8**, 158–165 (2021).
16. Pan A, Zhang Y, Wen K et al. Subwavelength resolution Fourier ptychography with hemispherical digital condensers. *Opt Express* **26**, 23119–23131 (2018).
17. Voigt FF, Kirschenbaum D, Platonova E et al. The mesoSPIM initiative: open-source light-sheet microscopes for imaging cleared tissue. *Nat Methods* **16**, 1105–1108 (2019).
18. Fan JT, Suo JL, Wu JM et al. Video-rate imaging of biological dynamics at centimetre scale and micrometre resolution. *Nat Photonics* **13**, 809–816 (2019).
19. McConnell G, Trägårdh J, Amor R et al. A novel optical microscope for imaging large embryos and tissue volumes with sub-cellular resolution throughout. *eLife* **5**, e18659 (2016).
20. McConnell G, Amos WB. Application of the Mesolens for sub-cellular resolution imaging of intact larval and whole adult *Drosophila*. *J Microsc* **270**, 252–258 (2018).
21. Schniete J, Franssen A, Dempster J et al. Fast optical sectioning for widefield fluorescence mesoscopy with the mesolens based on HiLo microscopy. *Sci Rep* **8**, 16259 (2018).
22. Lu RW, Sun WZ, Liang YJ et al. Video-rate volumetric functional imaging of the brain at synaptic resolution. *Nat Neurosci* **20**, 620–628 (2017).
23. Zong WJ, Wu RL, Li ML et al. Fast high-resolution miniature two-photon microscopy for brain imaging in freely behaving mice. *Nat Methods* **14**, 713–719 (2017).
24. Young MD, Field JJ, Sheetz KE et al. A pragmatic guide to multiphoton microscope design. *Adv Opt Photonics* **7**, 276–378 (2015).
25. Stirman J N, Smith I T, Kudenov M W et al. Wide field-of-view, multi-region, two-photon imaging of neuronal activity in the mammalian brain. *Nat Biotechnol* **34**, 857–862 (2016).
26. Yu CH, Stirman JN, Yu YY et al. Diesel2p mesoscope with dual independent scan engines for flexible capture of dynamics in distributed neural circuitry. *Nat Commun* **12**, 6639 (2021).
27. Sofroniew NJ, Flickinger D, King J et al. A large field of view two-photon mesoscope with subcellular resolution for in vivo imaging. *eLife* **5**, e14472 (2016).
28. Lu RW, Liang YJ, Meng GH et al. Rapid mesoscale volumetric

imaging of neural activity with synaptic resolution. *Nat Methods* **17**, 291–294 (2020).
29. Ota K, Oisi Y, Suzuki T et al. Fast, cell-resolution, contiguous-wide two-photon imaging to reveal functional network architectures across multi-modal cortical areas. *Neuron* **109**, 1810–1824.e9 (2021).
30. Diaspro A, Chirico G, Collini M. Two-photon fluorescence excitation and related techniques in biological microscopy. *Quart Rev Biophys* **38**, 97–166 (2005).
31. Svoboda K, Yasuda R. Principles of two-photon excitation microscopy and its applications to neuroscience. *Neuron* **50**, 823–839 (2006).
32. Kingslake R, Johnson RB. *Lens Design Fundamentals* 2nd ed 570 (Elsevier, Amsterdam, 2010).
33. den Dekker AJ, van den Bos A. Resolution: a survey. *J Opt Soc Am A* **14**, 547–557 (1997).
34. Dixon AE, Damaskinos S, Ribes A et al. A new confocal scanning beam laser MACROscope using a telecentric, f-theta laser scan lens. *J Microsc* **178**, 261–266 (1995).
35. Du E, Shen SH, Qiu A Q et al. Confocal laser speckle autocorrelation imaging of dynamic flow in microvasculature. *Opto-Electron Adv* **5**, 210045 (2022).
36. Liu S, Hua H. Extended depth-of-field microscopic imaging with a variable focus microscope objective. *Opt Express* **19**, 353–362 (2011).
37. Botcherby EJ, Smith CW, Kohl MM et al. Aberration-free three-dimensional multiphoton imaging of neuronal activity at kHz rates. *Proc Natl Acad Sci USA* **109**, 2919–2924 (2012).
38. Qi ZY, Guo QC, Wang S et al. All-fiber-transmission photometry for simultaneous optogenetic stimulation and multi-color neuronal activity recording. *Opto-Electron Adv* **5**, 210081 (2022).
39. Wang XY, Yao TY, Liu MK et al. A normalized absolute values adaptive evaluation function of image clarity. *Sensors* **23**, 9017 (2023).
40. Hu SR, Li ZY, Wang SH et al. A texture selection approach for cultural artifact 3D reconstruction considering both geometry and radiation quality. *Remote Sens* **12**, 2521 (2020).
41. Yang WJ, Yuste R. *In vivo* imaging of neural activity. *Nat Methods* **14**, 349–359 (2017).
42. Tomer R, Ye L, Hsueh B et al. Advanced CLARITY for rapid and high-resolution imaging of intact tissues. *Nat Protoc* **9**, 1682–1697 (2014).
43. Ueda HR, Ertürk A, Chung K et al. Tissue clearing and its applications in neuroscience. *Nat Rev Neurosci* **21**, 61–79 (2020).
44. Wu ST, Yang ZC, Ma CG et al. Deep learning enhanced NIR-II volumetric imaging of whole mice vasculature. *Opto-Electron Adv* **6**, 220105 (2023).

Acknowledgements

This study was supported by National Key R&D Program of China (grant no. 2022YFC2404201), the Chinese Academy of Sciences Project for Young Scientists in Basic Research (grant no. YSBR067).

Author contributions

G. H. Shi conceived the project. X. Xu, Q. Luo, J. X. Wang and H. Ye designed and built the optical setups. X. Xu, Y. H. Song, X. Zhang, Y. He and G. H. Shi designed and performed the experiments. M. X. Sun, R. B. Zhang, and H. Ye analysed the data. X. Xu, M. X. Sun and H. Ye wrote the paper with help of all authors.

Competing interests

The authors declare no competing financial interests.

Ethical statement

All experiments were performed according to Guidelines for Animal Experimentation of the Animal Experimentation Ethics Committee of the Suzhou Institute of Biomedical Engineering and Technology, Chinese Academy of Science.

Supplementary information

Supplementary information for this paper is available at https://doi.org/10.29026/oea.2024.230212

Scan for Article PDF